Nanoscale

PAPER

Environment-mediated structure, surface redox activity and reactivity of ceria nanoparticles

Thi X. T. Sayle,[a] Marco Molinari,[b] Soumen Das,[c] Umananda M. Bhatta,[d] Günter Möbus,[d] Stephen C. Parker,[b] Sudipta Seal[c] and Dean C. Sayle*[e]

Nanomaterials, with potential application as bio-medicinal agents, exploit the chemical properties of a solid, with the ability to be transported (like a molecule) to a variety of bodily compartments. However, the chemical environment can change significantly the structure and hence properties of a nanomaterial. Accordingly, its surface reactivity is critically dependent upon the nature of the (biological) environment in which it resides. Here, we use Molecular Dynamics (MD) simulation, Density Functional Theory (DFT) and aberration corrected TEM to predict and rationalise differences in structure and hence surface reactivity of ceria nanoparticles in different environments. In particular we calculate reactivity 'fingerprints' for unreduced and reduced ceria nanoparticles immersed in water and in vacuum. Our simulations predict higher activities of ceria nanoparticles, towards oxygen release, when immersed in water because the water quenches the coordinative unsaturation of surface ions. Conversely, in vacuum, surface ions relax into the body of the nanoparticle to relieve coordinative unsaturation, which increases the energy barriers associated with oxygen release. Our simulations also reveal that reduced ceria nanoparticles are more active towards surface oxygen release compared to unreduced nanoceria. In parallel, experiment is used to explore the activities of ceria nanoparticles that have suffered a change in environment. In particular, we compare the ability of ceria nanoparticles, in an aqueous environment, to scavenge superoxide radicals compared to the same batch of nanoparticles, which have first been dried and then rehydrated. The latter show a distinct reduction in activity, which we correlate to a change in the redox chemistry associated with moving between different environments. The reactivity of ceria nanoparticles is therefore not only environment dependent, but is also influenced by the transport pathway or history required to reach the particular environment in which its reactivity is to be exploited.

Introduction

Nanocrystalline cerium oxide is widely studied as a multifunctional material as it finds application in various fields including: catalysis,[1] solid oxide fuel cells,[2] polishing agents,[3] and bio-medical including: 'oxidase-like' activity,[4] superoxide radical scavenging[5] and oxygen modulation.[6] Most of these applications depend critically upon the surface reactivity of the CeO_2 nanocrystals. Specifically, how strongly each atom (Ce and O) is bound to the surface simultaneously governs the surface catalytic reactivity and the mobility of atoms, which in turn depends on the lattice orientation and faceting habit of the nanocrystal.[7]

For many applications, notably biomedical, the molecular environment or biological fluid in which it is immersed can have a profound influence over its surface reactivity.[8] In particular, Zhang and co-workers found[9] that a solvent, such as water, can even lead to a phase change in the nanoparticle; solvent is also pivotal to crystal morphology.[10]

'Nanoparticles combine the properties of a solid with the ability to move (a property of molecules)'.[11] Accordingly, owing to its solubility in a fluid, ceria nanoparticles can be transported in biological systems to a variety of environments. As the nanoparticle interacts within its environment, so its reactivity may change depending upon the environment in which it resides. For a living organism the environment can change considerably, from aqueous, spanning wide pH, to organic. If nanomaterials are to be used medicinally, then it is important to understand how the molecular environment might influence (desirable) surface reactivity.

[a]Department of Engineering and Applied Science, Cranfield University, Defence Academy of the United Kingdom, Shrivenham SN6 8LA, UK

[b]Department of Chemistry, University of Bath, Claverton Down, Bath, Avon BA2 7AY, UK

[c]Department of Mechanical, Materials and Aerospace Engineering, Advanced Materials Processing Analysis Center, Nanoscience Technology Center, University of Central Florida, Orlando, FL, USA

[d]NanoLAB Centre, Department of Materials Science and Engineering, Sheffield University, Sheffield S1 3JD, UK

[e]School of Physical Sciences, University of Kent, Canterbury, Kent, CT2 7NZ, UK. E-mail: d.c.sayle@kent.ac.uk

Ceria is widely exploited catalytically because of its ability to extract, store and release oxygen. Moreover, as one traverses to the nanoscale its catalytic reactivity is greatly enhanced. Oxygen modulation is central to many biological processes, and therefore the ability to modulate oxygen artificially (using, for example a nanoparticulate 'drug') represents a major advance. Owing to the small size of ceria nanoparticles, which can traverse the body, dissolved in biological fluids, ceria nanoparticles might prove ideal candidates to act as 'artificial oxygen modulators'.

Previously, we revealed that ceria nanoparticles can indeed extract, store and release oxygen in targeted biological environments.[6] In particular, we showed how nanoceria can be used to promote angiogenesis using *in vitro* and *in vivo* experimentation supported by atomistic computer simulation data. Specifically, the experiments and simulations revealed that the reactivity of oxygen on the surface of the nanoceria and therefore its ability to release and accept oxygen, was key to such remarkable behaviour. However, the atomistic simulations used to calculate the energy associated with extracting oxygen from the surface of the ceria nanoparticle were performed in vacuum. Such simulations are necessarily simplistic because they do not account for how the (biological fluid) environment will influence the lability of surface oxygen and hence the propensity for the nanoparticle to release oxygen. Accordingly, more realistic simulations are required, which account for the molecular environment in which the nanoparticles reside.

Here, we use atomistic simulation in combination with experiment to elucidate at the atomistic level, phenomenon that influence nanoparticle surface reactivity and whether simulation can be used to predict how the properties and reactivity of a nanoparticle might change as a function of environment.

Molecular Dynamics (MD) simulation is used to generate full atomistic models of ceria nanoparticles immersed in water and in vacuum and their relative structures and activities calculated. In particular, we calculate chemical reactivity 'fingerprints' for the nanoparticles following ref. 12 in water and in vacuum to ascertain the influence of the molecular environment in which the nanoparticle is immersed. The reactivity fingerprints involve colouring each atom comprising the nanoparticle as a function of how strongly it is bound to the nanoparticle; weakly bound atoms are energetically more easily extracted from the surface to participate in, for example, an oxidation reaction. In this study, a red-white-blue gradiented scale is used to reflect low to high binding energies respectively.

In parallel, we synthesise real nanoparticles and compare the properties of the as-synthesised ceria nanoparticles (CNP) with the same batch of nanoparticles that have been dried and rehydrated (R-CNP). In particular, we measure the activity of CNP and R-CNP towards scavenging superoxide radicals and correlate the differences in activities with changes in the redox chemistries of the nanoparticles.

Methods

In this section we detail the potential model used to describe the ceria nanoparticles and water together with nanoparticle–water interactions; the computer code used to perform the molecular dynamical simulations; methods used to generate fully atomistic models of the ceria nanoparticles and methods for synthesising and characterising ceria nanomaterials experimentally.

Potential models

A rigid ion potential model, with partial charges, is used to represent the CeO₂ lattice. The potential model comprises long-range Coulomb interactions, short-range interactions described using a Morse function form and a further short-range repulsive contribution following:

$$U(r) = \frac{z_i z_i e^2}{r} + D_{ij}\left[\left\{1 - e^{-a_{ij}(r - r_0)}\right\}^2 - 1\right] + \frac{C_{ji}}{r^{12}}, \qquad (1)$$

where U is the lattice energy, z the charge on ions i and j, r the interatomic distance between i and j and r_0 the equilibrium bond distance between atoms i and j.

The potential is a modification of an empirical potential model derived by Pedone *et al.*[13] with short range cation–cation interactions set to zero; the potential parameters are given in Table 1.

The potential models, used to describe the interactions between CeO₂ and water, were derived using relaxed fitting using structures derived from first principle calculations;[14] structural data from experiment is as yet unavailable. The structural models used to fit the potential include: CeO₂{111}, {110} and {100} surfaces with associatively adsorbed water. The potential was fitted to a Lennard-Jones '9-6' functional form and the parameters are listed in Table 2. The water solvent is described using the flexible rigid ion TIP3P as found in Cornell *et al.*[15]

Simulation codes

The GULP code was used to perform the relaxed fitting of the potential parameters and to calculate the defect energies,[16] the METADISE code to calculate surface and adsorption energies[17] and the DL_POLY code to perform all the molecular dynamics (MD) simulations.[18] The DL_POLY user manuals provide

Table 1 Potential parameters of the form: $U(r) = D_{ij}[\{1 - e^{-a_{ij}(r-r_0)}\}^2 - 1] + \frac{C_{ji}}{r^{12}}$

Species	D_{ij} (eV)	a_{ij} (Å⁻²)	r_0 (Å)	C_{ij} (eV Å¹²)
Ce²·⁴–O⁻¹·²	0.098352	1.848592	2.930147	1
O⁻¹·²–O⁻¹·²	0.041730	1.886824	3.189367	22
Ce¹·⁸–O⁻¹·²	0.000200	1.924002	4.482585	3

Table 2 Potential parameters for the Lennard-Jones 9-6 short-range potential

Species	A (eV Å⁹)	B (eV Å⁶)
Ce²·⁴–OW⁻⁰·⁸³⁴	3248.194052	180.100177
O⁻¹·²–OW⁻⁰·⁸³⁴	3136.832265	32.444380
Ce¹·⁸–OW⁻⁰·⁸³⁴	3248.194052	180.100177

comprehensive analytical descriptions and discussion of the energy minimization calculations and molecular dynamics simulations, force fields, boundary conditions, algorithms and parallelisation methods used in these simulations. Analysis of the atomistic models using molecular graphics, were performed using VMD,[19] Materials Studio and VESTA.[20]

Atomistic model generation

To generate atomistic models of ceria nanoparticles, a particle of ceria was first amorphised and then crystallised in vacuum and in water. In particular, a real ceria nanoparticle is structurally complex in that it comprises the crystal structure together with microstructural features, which include, for example: morphology and surfaces exposed (steps, edges and corners), dislocations, grain-boundaries and point defects. Moreover, it is well known that the microstructure of a material governs its properties. Accordingly, if one is to generate an atomistic model, which is used to interrogate its properties in reliable accord with experiment, then this structural complexity must be captured within the structural model – including synergistic interactions between microstructural features. Traditionally, symmetry operators have been used to construct atomistic models and the surfaces of the nanoparticle introduced by cleaving the crystal. However, introducing microstructural features is more problematic. In particular, while dislocations and grain-boundaries have been introduced into atomistic models in isolation – normally in the parent bulk material – to introduce dislocations, grain-boundaries and point defects, steps, edges, corners and quench surface dipoles within a nanoparticle, together with their synergy of interaction is a challenging undertaking. Accordingly, we propose that the easiest way to generate an atomistic model that is in structural accord with experiment is to simulate the synthetic method of fabrication. Typically, synthesis involves some kind of crystallisation step, which evolves the complex microstructures observed. Accordingly, by simulating crystallisation, we are able to capture atomistic models, which include complex microstructures.

To this end a cube of ceria comprising 15 972 atoms was cleaved from the parent bulk material and melted under constant volume MD simulation at 6500 K and immersed in water. In particular 27 909 water molecules were introduced into the simulation cell and NPT† MD simulation run at 2400 K for 1500 ps with a pressure of 1 GPa to ensure liquid-phase water with a density of about 1 g cm^{-3}. The system was then cooled to 300 K (77 ps at 1 GPa pressure, then 35 ps at 0.001 GPa pressure) and finally 1 K (5 ps at 0.001 GPa pressure). The water was then removed and constant volume MD simulation performed for a further 50 ps at 1 K. A timestep of 0.001 ps was used throughout. The simulation required 50 000 cpu hours.

To generate atomistic models for ceria nanoparticles crystallised in vacuum, constant volume NVT‡ MD simulation was performed (without water) using the amorphous precursor for 7 ns at 1800, 2000, 2200, 2400, 2600 and 2800 K (at 2200 K the system was only run for 2 ns because energy convergence had been reached after this time). Three-dimensional periodic boundary conditions were imposed in all calculations.

Redox chemistry

To explore the redox chemistry of ceria nanoparticles, the nanoparticle crystallised in water was reduced by randomly replacing: 100, 500 and 2000 Ce^{4+} species for Ce^{3+}; charge neutrality was maintained by creating 50, 250 and 1000 oxygen vacancies respectively, located at random positions. The reduced nanoparticles are therefore commensurate with Ce^{3+}/Ce^{4+} ratios of 0.02 (100 Ce^{3+}), 0.1 (500 Ce^{3+}) and 0.6 (2000 Ce^{3+}). Each reduced nanoparticle was then equilibrated under constant pressure in water at 300 K for 0.1 ps. NPT simulation was then performed in water for 1 ps at 300 K and then 5 ps at 1 K. The nanoparticles were then 'dried' by removing the water and performing NVT simulation at 1 K for 5 ps.

Reactivity fingerprints

The (oxidative catalytic) reactivity of ceria surfaces is intuitively dependent upon the ease of extracting oxygen from the surface of the oxide and can be gauged by calculating oxygen vacancy formation energies. This well-established technique, is detailed in ref. 21. Reactivity 'fingerprints' can therefore be generated by calculating the vacancy formation energies of all atoms comprising the nanoparticle. However, for typical nanoparticles, comprising in excess of 15 000 atoms, such a calculation is prohibitively expensive. Migani and co-workers recently showed[22] that the 'oxygen vacancy formation energy is driven by the electrostatics, thus enabling the prediction of the most easily removable oxygen atoms by analyzing the distribution of the electrostatic potential in the pristine stoichiometric (vacancy-free) ceria systems'. Moreover, previously we showed that the electrostatic potential correlates with the vacancy formation energy.[12] Calculating the electrostatic potential of each atom is seven orders of magnitude computationally less expensive compared to vacancy formation energy calculations, which enables a computationally tractable method for generating nanoparticle reactivity maps. Accordingly, we use this technique to present reactivity 'fingerprints' of the ceria nanostructures.

Experiment

Cerium oxide nanoparticles were synthesized using a micro emulsion method;[23] 30% ammonium hydroxide was added to precipitate the nanoparticles from toluene. The particles were then washed with acetone and water to remove the surfactant and other impurities and suspended in deionized water (CNP). One portion of the nanoparticles was then dried, under vacuum, at 60 °C for 24 h and re-hydrated in the same volume of deionised water (R-CNP).

The catalytic activities of CNP's and R-CNP's were then gauged by comparing their propensity to scavenge superoxide radicals[5] as determined using a WST1 dye (2-(4-iodophenyl)-3-(4-nitrophenyl)-5-(2,4-disulfo-phenyl)-2*H*-tetrazolium, monosodium

---

† NPT: constant Number of particles, constant Pressure and constant Temperature.

‡ NVT: constant Number of particles, constant Volume and constant Temperature.

salt). In particular, superoxide radicals will reduce soluble (WST1) tetrazolium salts to (WST1) formazan; the reduction kinetics can be determined by monitoring the colour change (at 440 nm) associated with the reduction. In particular, the ceria nanoparticles can scavenge the superoxide radical and inhibit the reduction. The activity of the nanoparticles towards radical scavenging can therefore be estimated by measuring the inhibition rate as determined by measuring the colour change (absorbance at 440 nm) as a function of time. The rate of inhibition of the WST1 formazan (superoxide mimetic reactivity) was calculated following:

SOD activity (inhibition rate %) =

$$\frac{(A_{blank1} - A_{blank3}) - (A_{sample} - A_{blank2})}{A_{blank1} - A_{blank3}} \times 100, \quad (2)$$

where A_{blank1} – absorption in control with deionized water, A_{blank2} – without enzyme and with sample, A_{blank3} – without enzyme and with deionized water and A_{sample} – with sample and enzyme.

Abberation corrected TEM was used to characterise ceria nanoparticles with atom-level clarity. Near-surface regions of a hydrothermally prepared ceria nanoparticle[24] were imaged and quantified for site occupancy using 300 keV aberration corrected TEM (JEM 3100 R005, University of Sheffield). Spherical aberration and defocus values close to zero have the advantage of suppressing carbon-support film contrast and avoiding Fresnel fringes which would disturb visibility of finest surface reconstruction details as described in ref. 7. Real-time video recording at a rate of 30 fps (Gatan ORIUS digital video & CCD camera) is used here to analyse irradiation induced surface reactivity, such as Ce-hopping or formation/ablation of entire monolayers.

Results

In this section we describe how well the potential model fits to experiment, the simulated crystallisation of ceria nanoparticles in vacuum and in water, calculated reactivity 'fingerprints' of the ceria nanoparticles in vacuum and immersed in water and finally the measured redox chemistry.

Potential model

Calculated structural parameters, compared with experiment, are reported in Table 3 and the energies of various intrinsic disorder reactions in CeO_2 bulk and the oxygen migration energy barrier in Table 4. Experimental and simulation data – the latter using different potential models – can be found in ref. 25–27 and references therein.

The relative stability of the relaxed three low Miller index CeO_2 surfaces, Table 5, decreases in the order {111}, {110} and {100} in accord with previous density functional theory, for example see ref. 14 and references therein. Conversely, the relative adsorption energies for a single water molecule increases in the order CeO_2{111}, {110} and {100} again in relative accord with DFT.[14]

Table 3 Comparison of predicted properties with experiments

	Lattice parameters			
	$a = b = c$ (Å)	$\alpha = \beta = \gamma$ (deg)	Ce–O (Å)	O–O (Å)
Exp.	5.411	90	3.826	2.343
Calc.	5.412	90	3.827	2.343

	Elastic constants (GPa)			
	C_{11}	C_{12}	C_{44}	Bulk modulus
Exp.	403	105	60	204–236
Calc.	404	94	83	197

Table 4 Energies (eV) per defect for disorder reactions and barrier for oxygen migration

	Schottky	Cation Frenkel	Anion Frenkel	Oxygen migration barrier
This work	4.95	9.95	3.25	0.55
Other simulations	3.33–5.79	8.86–15.94	2.81–4.24	0.3–0.74
Exp.				0.52–0.7

Table 5 Calculated surface energies of the low index ceria surfaces together with calculated adsorption energies of (single) water molecule onto these low index surfaces

	Surface energy (J m^{-2})		Water adsorption energy (kJ mol^{-1})	
Surface	This work (atomistic)	DFT	This work (atomistic)	DFT
$CeO_2(111)$	1.39	0.71	−39	−56
$CeO_2(110)$	2.03	1.06	−77	−82
$CeO_2(100)$	2.72 (2.68)	1.44	−135 (−94)	−96

We note that for (dipolar type III) CeO_2{100} surfaces, different structures with similar surface energies were obtained, Table 5. In particular, the oxygen sublattice undergoes a strong relaxation in both cases, Fig. 1, but while in the first case, Fig. 1(a) and (b) the 2-fold surface oxygen ions occupy regular surface lattice site to yield a surface energy of 2.72 J m^{-2}, in the second, Fig. 1(c) and (d), they shift 0.6 Å from their regular surface lattice site to accommodate a zigzag configuration and a slight reduction in surface energy to 2.68 J m^{-2}. This causes a shift inwards and a contraction of the Ce–O distance of 7.35% (Fig. 1(a) and (b)) and 4.97% (Fig. 1(c) and (d)). The second and third oxygen layers in both cases are also split as reported previously by Nolan et al.[28]

We also report two water adsorption energies on $CeO_2(100)$. This emanates from two different configurations identified for water adsorption on this surface. In particular, one
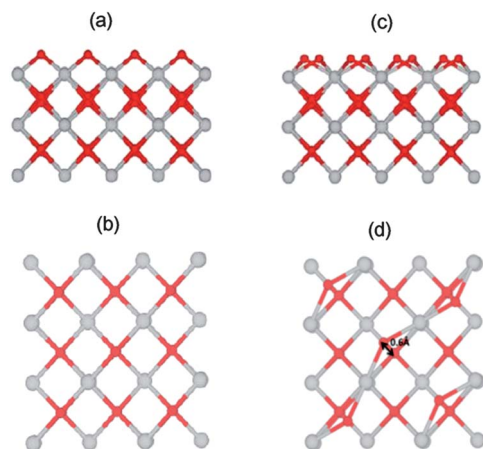
Fig. 1 CeO$_2${100} relaxed surface with regular lattice (left) and zigzag (right) surface oxygen ions; oxygen are coloured red and cerium, grey.

configuration involves water shifting an entire array of surface oxygen (-94 kJ mol^{-1}). Conversely, the other configuration involves only part of the O surface array shifted with another part remaining in the original zigzag position (-135 kJ mol^{-1}). Such structural differences are a consequence of quenching the dipole associated with fluorite{100} surfaces, which is achieved by filling only 50% of the surface oxygen sites.

Simulated crystallisation in vacuum

Analysis of the simulated crystallisation process, using molecular graphics, of the nanoparticle crystallised in vacuum at 2200 K, revealed the spontaneous evolution of multiple crystalline seeds, Fig. 2(a), conforming to the fluorite structure and exposing {111} at the surface. The seeds nucleated the crystallisation of the surrounding amorphous sea of ions and agglomerated, *via* an 'Ostwald ripening' mechanism, to yield a single octahedral crystal, Fig. 2(b) and (c) with {111} surfaces truncated by {100} and {110} in accord with experiment, Fig. 2(d). One might consider the {110} surfaces to be steps on the {111}. However, the area of these 'steps' is sufficiently large to consider them to be a surface rather than a step.

Close inspection of the 'Ostwald ripening' mechanism, using molecular graphics revealed that atoms at the interface between the two misoriented grains moved from the surface of one grain to extend the surface of the other grain and thus increase its size, while the other grain reduces in size and is eventually assimilated. The mechanism was concerted involving several atoms at a time and therefore not wholly atom-by-atom; rather a layer-by-layer movement of ions was observed with sections of each layer moving from one grain to the other analogous to a zip like mechanism.

For the nanoparticles crystallised in vacuum at all other temperatures (not shown), the (mis-oriented) crystalline regions did not fully agglomerate (Ostwald ripen) into a single crystal within the duration of the MD simulation. Accordingly, the nanoparticles remained polycrystalline with a variety of grain-boundaries. We note that at 2800 K the nanoparticle failed to
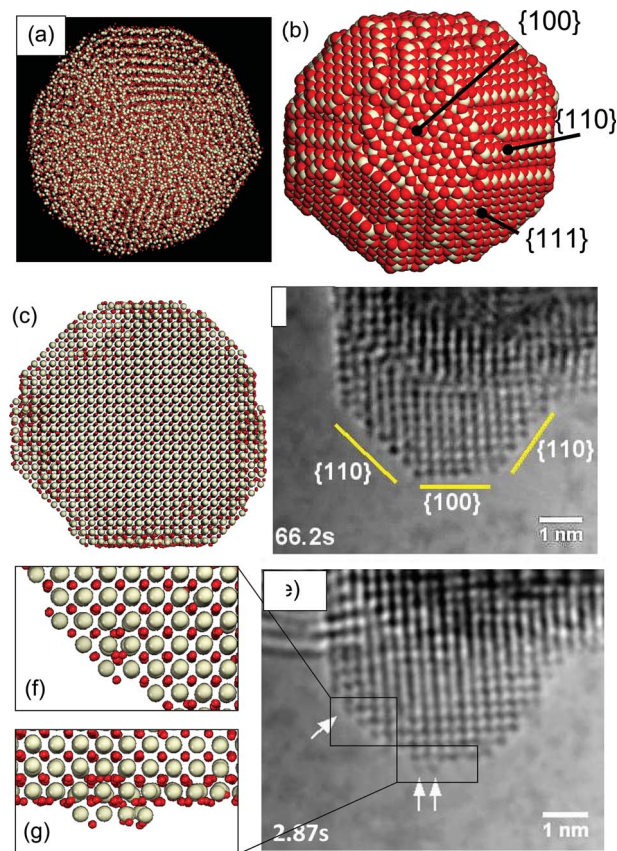
Fig. 2 Model atomistic structure and HRTEM images of ceria nanoparticles. (a) snapshot of a nanoparticle that has part-crystallised; four crystalline seeds are evident from the figure. (b) low temperature model structure after full crystallisation showing the surfaces exposed. (c) as (b) but with smaller spheres revealing that the nanoparticle is a single crystal. (d) HRTEM image of a ceria nanoparticle revealing the {110} and {100} surfaces to compare and validate the model in (c). (e) an earlier image of (d) showing atom clusters on the {110} and {100} surfaces (arrows), which are also observed in the atomistic model (f) and (g); the clusters reconstruct to facilitate planar surfaces (d). Cerium atoms are coloured white and oxygen is red.

crystallise and remained molten. We now consider the nanoparticle, crystallised at 2200 K, in more detail:

Analysis of the nanoparticle using molecular graphics, revealed the presence of atom clusters on the surface. In particular, Fig. 2(f) and (g) show respectively atom clusters on the {110}: Fig. 2(f) and {100}: Fig. 2(g) surfaces, similar to those observed experimentally, Fig. 2(e). The evolution of such structural features are a consequence of simulating crystallisation. Specifically, simulated amorphisation and crystallisation is able to capture, within the atomistic models: the crystal structure, morphology and surface exposed (steps, edges and corners) together with detailed microstructural features including grain-boundaries, dislocations and atom clusters on the surface within a single model. Conversely, if the models were generated using symmetry operators (to cleave the {111}, {110} and {100} surfaces), the models would necessarily be more pristine and we argue, less representative of real nanoparticles.

We note that the HRTEM images, Fig. 2(d) and (e) do not resolve oxygen ions because of the considerable difference in

atomic number of Ce and O; rather only cerium ions are resolved. This illustrates the synergies with atomistic simulation. In particular, the model can be checked to see whether it evolves to give the same cerium atom positions as identified experimentally and then used to predict the location of oxygen atoms comprising the clusters, Fig. 2(f) and (g). In future this strategy may represent an experimental approach for computing oxygen positions. We note that oxygen ions have been resolved in TiO$_2$ using aberration corrected TEM.[29]
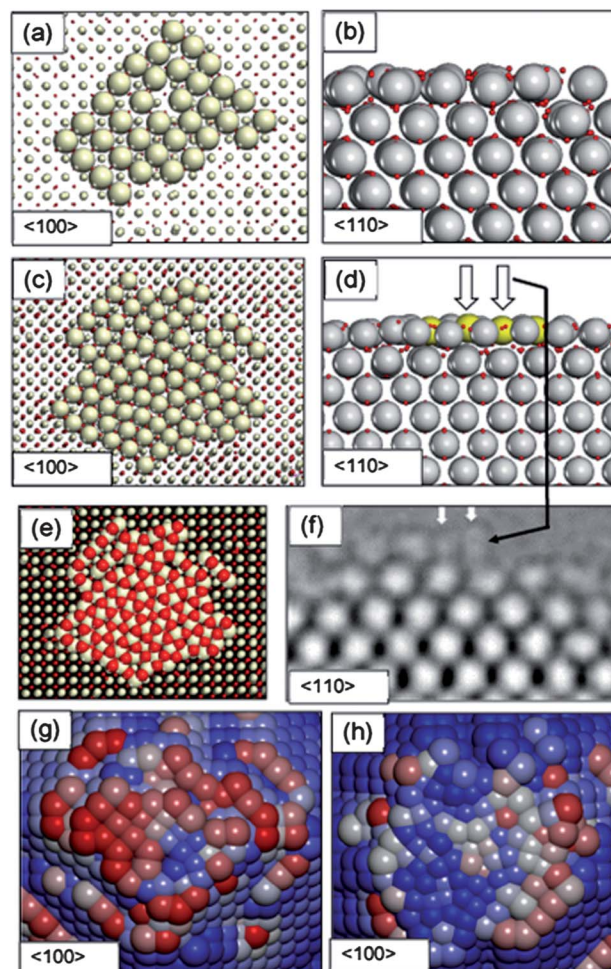
Analysis of the {100} surfaces of the nanoparticle reveal Ce ions, comprising the surface atomic layer, located on lattice sites and, perhaps surprisingly, interstitial positions. In particular, on one particular {100} surface, the Ce atoms are located predominantly on lattice sites, Fig. 3(a) and (b) and on another {100} surface, Ce are observed at interstitial (octahedral) positions, Fig. 3(c)–(e). Both are observed experimentally, Fig. 3(f). Our models are therefore in quantitative agreement with experiment and capture not only the crystal structure and morphology, but also structural detail down to the level of individual atoms on the surface occupying non-lattice sites. We therefore suggest that our potential models and methodology are accurate in describing the structure of ceria and can be applied with confidence to explore the structure of ceria crystallised in water.

CeO$_2${100} surfaces have been shown experimentally to be catalytically more reactive compared to, for example, CeO$_2${111}, and are therefore subject to much interest. In particular fluorite-structured {100} surfaces are dipolar[30] and to facilitate stability, must undergo a structural rearrangement to quench the surface dipole. It is therefore interesting to determine whether the two types of surface reconstruction observed in the models (surface Ce at lattice or interstitial sites) proffer different reactivities. Accordingly, we calculated the electrostatic potential of surface oxygens occupying predominantly lattice sites, Fig. 3(g), compared to surface oxygens occupying predominantly interstitial sites, Fig. 3(h). A comparison between the two, reveals that the electrostatic potentials of surface oxygen occupying lattice sites are markedly lower (and hence more reactive) compared to interstitial surface oxygens. We attribute this behaviour to the higher packing density of ions occupying interstitial sites, which is evident by comparing Fig. 3(a) and (c).

Fig. 3 Model atomistic structures and HRTEM images of the {100} surfaces of a ceria nanoparticle. (a) View looking along ⟨100⟩ revealing the uppermost atomic ceria layer with Ce occupying ceria lattice sites; (b) side ⟨110⟩ view of (a), (c) view looking along ⟨100⟩ revealing the uppermost atomic ceria layer with Ce occupying interstitial and lattice positions, (d) side ⟨110⟩ view of (c) revealing more clearly the Ce ions (yellow) occupying interstitial sites, (e) as (c) but showing oxygen atoms in the top atomic layer, (f) HRTEM image revealing Ce atoms located at lattice and interstitial sites in the top atomic layer, (g) as (a) with oxygen atoms, coloured according to electrostatic potential, (h) as (c) with oxygen atoms, coloured according to electrostatic potential. Cerium is coloured white and oxygen is red. Low to high electrostatic potentials are represented respectively by a red-white-blue gradiented scale.

Simulated crystallisation in water

Analysis, using molecular graphics, of the (simulated) crystallisation process of the nanoparticle immersed in water reveals the spontaneous evolution of multiple fluorite-structured crystalline seeds within the amorphous sea of ions, Fig. 4(a)–(c). In particular, Fig. 4(a) shows the atom positions of the nanoparticle in which a crystalline seed has evolved, 4(b) is an enlarged segment of 4(a) revealing more clearly the (highly disordered) fluorite-structured crystalline region, 4(c), which extends to the surface exposing {111}.
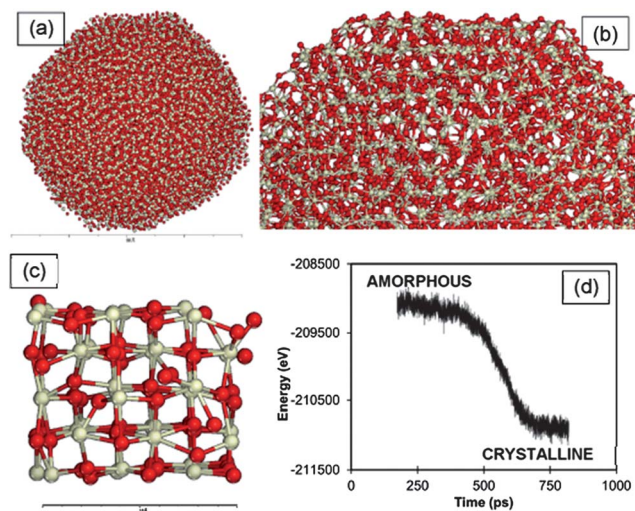
As crystallisation proceeds, the seeds nucleate crystallisation of the surrounding amorphous sea of ions. Moreover, as the crystallisation fronts, emanating from the (mis-oriented)

crystalline seeds impinge upon one another, grain-boundaries are formed. The individual seeds then agglomerate together, *via* an Ostwald ripening mechanism, to yield larger crystalline regions. The assimilation of small grains by larger grains was shown previously by us in ref. 31. Analysis, using molecular graphics of the ripening process (not shown) revealed a layer-by-layer realignment of the Ce atom positions, which occurs at the grain-boundary regions as one crystalline grain consumes its neighbour analogous to the behaviour of the nanoparticle crystallised in vacuum.

The configurational energy of the system, calculated as a function of time, is shown in Fig. 4(d). From 0 to 250 ps, the nanoparticle is amorphous. However, after about 250 ps,
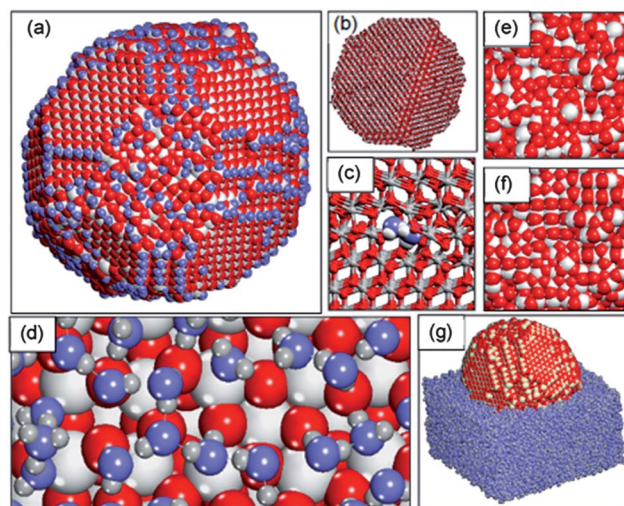
Fig. 4 Atom positions comprising a ceria nanoparticle, immersed in water (not shown) after a crystalline seed has spontaneously evolved. (a) Whole nanoparticle, (b) segment of (a) showing more clearly the crystalline seed, which exposes {111} at the surface, (c) segment of (b) showing more clearly the fluorite structure, (d) configurational energy (eV) calculated as a function of time (ps) showing that the crystallisation process is associated with a gradual reduction (more stable) in energy.

Fig. 5 Ceria nanoparticle immersed in water. (a) sphere model representation of the atom positions together with water molecules that reside closest to the nanoparticle (only the oxygen atom of the water is shown for clarity). (b) stick model representation revealing that the nanoparticle is a bi-crystal with a grain-boundary traversing through the particle and includes, (c), two water molecules trapped in the grain-boundary region. (d) sphere model representation of the atom positions showing the first layer of water molecules above a segment of a {100} surface. (e) plan view of one of the CeO_2{100} surfaces (water not shown). (f) same as (e) after removing water illustrating the subtle change in structure. (g) view of the nanoparticle immersed in the water; some of the water has been removed to enable visibility of the nanoparticle. Cerium is coloured white, oxygen (CeO_2) is red, oxygen (water) is blue and hydrogen, grey.

crystalline seeds spontaneously evolve within the amorphous sea of ions and nucleate crystallisation of the surrounding sea of Ce and O ions. As crystallisation proceeds the configurational energy reduces and crystallisation can be seen to occur from about 250 to 750 ps after which the configurational energy converges again. The energy difference between the two plateaus reflects loosely the heat of crystallisation.
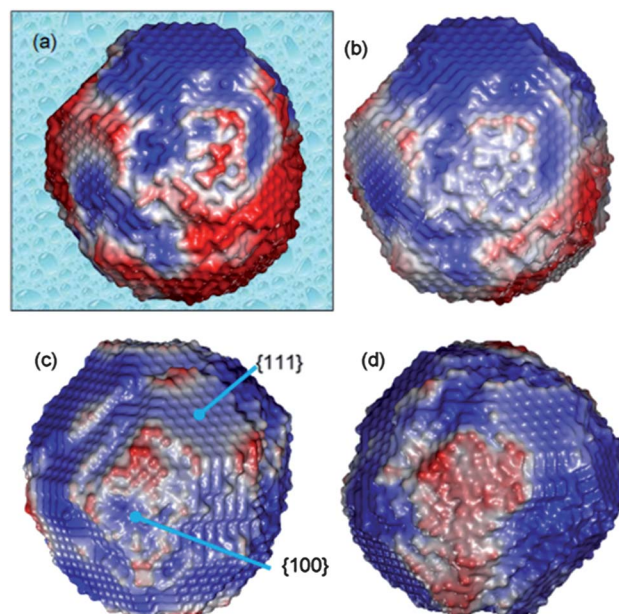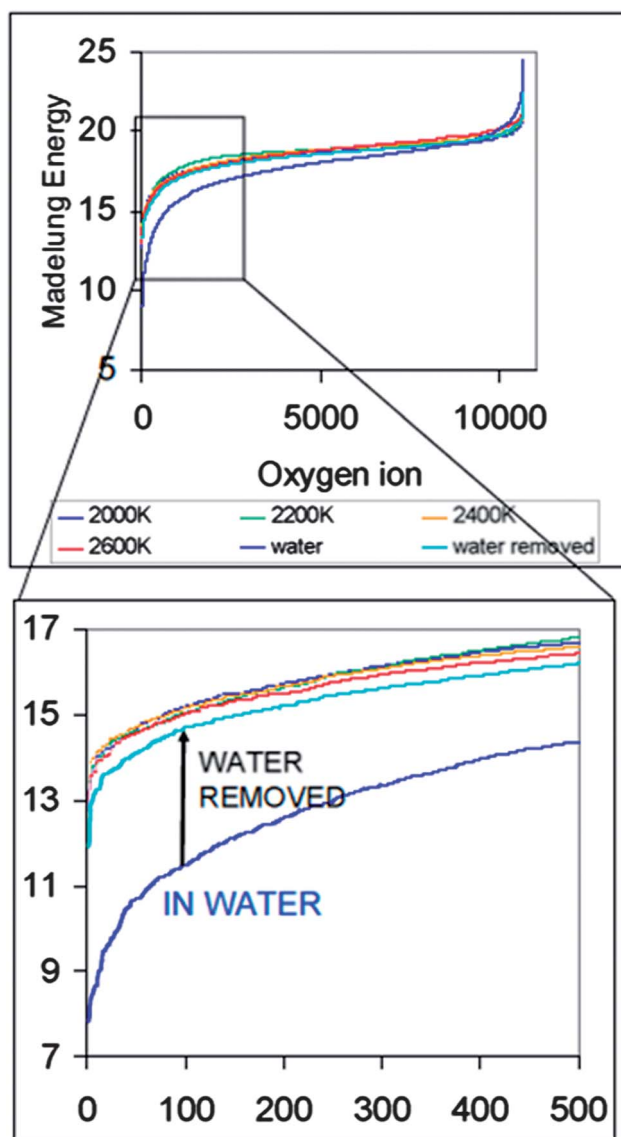
At the end of the crystallisation, similar to the nanoparticles crystallised in vacuum, the water-crystallised nanoparticle is an octahedron with {111} facets truncated by {100} and {110}, Fig. 5(a). A grain-boundary runs through the nanoparticle (Fig. 5(b)). We also note that two water molecules have become trapped within the GB region of the nanoparticle, Fig. 5(c). The grain-boundary conforms to Σ3 {111}/[110] and has been observed experimentally.[32]

The model structure together with water molecules closest (within 2.3 Å) to the surface of the nanoparticle, Fig. 5(a), reveals that the water molecules approach closest to low coordinated Ce. In particular the water decorates steps, edges, {100} and {110} surfaces. Conversely, the water does not approach as close to the {111} surfaces. We attribute this behaviour to the water aiding the stability of (potentially unstable) step/edge and {100}, {110} surfaces by increasing the coordinative saturation of Ce ions at these positions. An enlarged segment of water molecules in close proximity to a {100} surface, Fig. 5(d), reveals that the oxygen and hydrogen atoms of the water reside close to Ce and O atoms respectively of the ceria nanoparticle.

A further simulation was performed to explore whether the nanoparticle would change structurally if it were dehydrated resulting in a reduction in the coordinative saturation of surface Ce and O atoms. To this end, the water was removed and the

Fig. 6 Surface rendered models of ceria nanoparticles crystallised in water (a and b) and vacuum (c and d). The surface is coloured according to calculated electrostatic potential revealing more clearly reactive (red) compared to unreactive (blue) regions on the nanoparticle. (b) is as (a) but after the water had been removed. (c) Nanoparticle crystallised in vacuum at 2200 K and (d) 2400 K. Low to high electrostatic potentials are represented respectively by a red-white-blue gradiented scale; the more reactive areas are red.

atoms moved to low energy configurations by performing MD simulation at 1 K on the dehydrated nanoparticle; low-temperature MD simulation acts as a pseudo energy minimiser. The structure of the {100} before and after the water had been removed are shown in Fig. 5(e) and (f). Comparing the hydrated 5(e) and dehydrated 5(f) {100} surface reveals that dehydration causes subtle structural modifications of the surface ions. In particular, the Ce atoms relax deeper into the {100} surface of the nanoparticle to help quench the reduction in coordination number (as previously furnished by water). The structure of the nanoparticle immersed in water is shown in 5(g); the top half of the water molecules in the simulation cell have been removed to improve clarity.

Analysis of calculated Ce–O radial distribution functions (not shown) and measuring pertinent Ce–O distances of surface atoms, revealed that Ce–O bond distances, calculated for atoms on the surfaces of the nanoparticles, are generally smaller for the nanoparticle in vacuum compared to Ce–O bond distances associated with the nanoparticle immersed in water.

Reactivity

The reactivity 'fingerprints', calculated for the ceria nanoparticle crystallised in water is shown in Fig. 6(a) together with the corresponding reactivity map after removing the water, Fig. 6(b). Reactivity maps for ceria nanoparticles crystallised in vacuum at 2200 K and 2400 K are shown in Fig. 6(c) and (d) to compare. The reactivity map for 6(a) shows more red compared to 6(b) indicating that water immersion increases the reactivity in that it is energetically easier to extract oxygen from the surface. We also note that the nanoparticle crystallised in water, Fig. 6(a), is also more active compared to those in vacuum, Fig. 6(c) and (d).
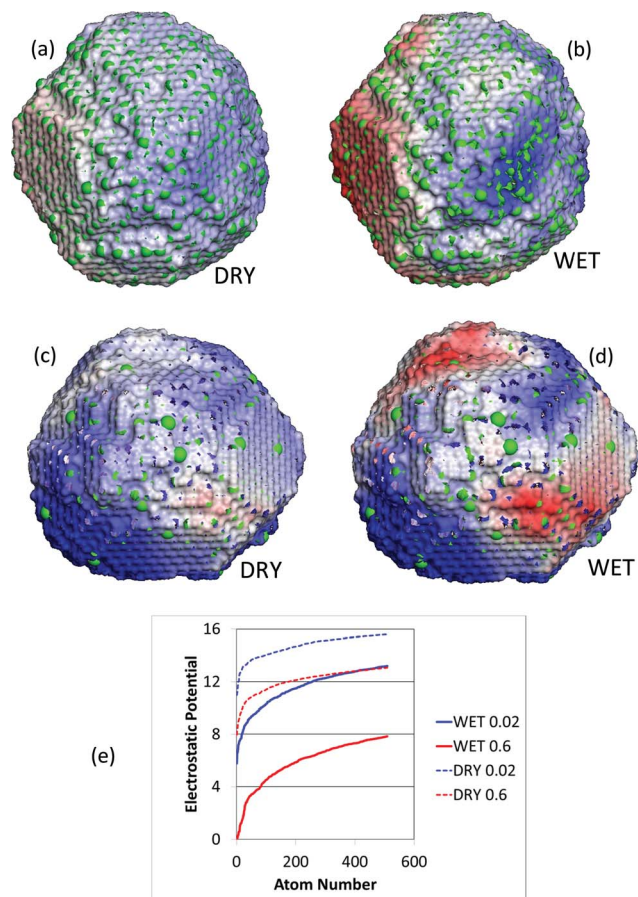

Fig. 7 Electrostatic potential (Madelung energies), calculated as a function of atom number, for all oxygen atoms comprising the ceria nanoparticles. The thin lines correspond to nanoparticles crystallised in vacuum spanning 2000–2600 K and the thick dark blue line, for the nanoparticle crystallised at 2400 K in water. The thick light blue line is for the nanoparticle crystallised in water but after the water had been removed.

Fig. 8 Activity fingerprints calculated for wet and dry ceria nanoparticles. (a) Dry and (b) wet ceria nanoparticles with Ce^{3+}/Ce^{4+} ratio of 0.6. (c) Dry and (d) wet ceria nanoparticles with Ce^{3+}/Ce^{4+} of 0.02. (e) Calculated (lowest 500) electrostatic potentials of oxygen comprising the ceria nanoparticles (a–d). The atomistic models for the ceria nanoparticles are shown with surface rendering coloured according to oxygen electrostatic potential. Low to high electrostatic potentials are represented respectively by a red-white-blue gradiented scale; the more reactive areas are red. The green spheres indicate the positions of Ce^{3+} species.

The electrostatic potential, calculated for all 10 648 oxygen ions comprising each nanoparticle, are shown in Fig. 7. The oxygen atoms with lowest electrostatic potential (most reactive) are, unsurprisingly, located at the surface. The figure reveals that the electrostatic potentials are reduced considerably for the nanoparticle immersed in water indicating that water immersion increases the surface reactivity. We also note that even after removing water, the electrostatic potentials are subtly lower compared to the ceria nanoparticles crystallised in vacuum, Fig. 7.

Redox chemistry

The activity fingerprints for the reduced ceria nanoparticles are shown in Fig. 8(a)–(d). The images reveal that the nanoparticles are more active towards the release of surface oxygen when immersed in water compared to the same nanoparticle when dry. The electrostatic potentials calculated for oxygen atoms comprising each of the four nanoparticles are shown in Fig. 8(e). Only 500 oxygen atoms with the lowest electrostatic potentials are shown to reveal those oxygen species that are easiest to extract. Perhaps unsurprisingly, all oxygen atoms with low electrostatic potential were found (using graphical techniques) to reside on the surface of the nanoparticle. Fig. 8(e) reveals that the degree of reduction (Ce^{3+}/Ce^{4+} ratio) of the ceria

nanoparticles plays a key role in their activity towards oxygen release. In particular, the highly reduced nanoparticles ($Ce^{3+}/Ce^{4+} = 0.6$) are more active towards oxygen release compared to the nanoparticle with $Ce^{3+}/Ce^{4+} = 0.02$.

Superoxide radical scavenging activity

In the final section we explore experimentally how the reactivity of ceria nanoparticles change as a consequence of changing (molecular) environment in which they reside.

Fig. 9 shows the measured inhibition of (WST1) tetrazolium salts to (WST1) formazan using CNP (non-dried) and R-CNP (dried-rehydrated) and reveals that as-prepared CNP are more effective inhibitors and therefore more active towards superoxide radical scavenging compared to the dried-rehydrated ceria nanoparticles. Specifically, the inhibition rates (eqn (2)) of the WST1 formazan formation (superoxide dismutase activity) were 20% and 8% for non-dried and dried rehydrated cerium oxide nanoparticles, respectively.

A possible explanation of this behaviour is that the concentration of surface Ce^{3+} is higher in CNP compared to R-CNP.[6] This is supported by UV-Visible spectroscopy. In particular, R-CNP nanoparticles show a red shift as compared to CNP, Fig. 8(b); characteristic edges of Ce^{3+} and Ce^{4+} absorbance are 258 nm and 298 nm, respectively. In particular, our experiments reveal that the solvent and solvent history can influence the redox chemistry and activity of ceria nanoparticles.

Discussion

It is important to understand why nanoparticles in water are calculated to be more active, such that this phenomenon can be exploited in future to facilitate tuneable reactivity and to be able to predict the reactivity of nanoparticles as a function of environment. Here we predict subtle changes in surface structure, which impacts upon the reactivity. In particular, for a nanoparticle in vacuum, surface Ce ions at low-coordinated (step, edge, corner and apical) sites relax into the surface of the nanoparticle to help saturate their coordination. Consequently, the Ce–O bond distances are typically shorter compared to (2.34 Å) Ce–O bond distances in the bulk of the nanoparticle. Conversely, Ce–O bond distances at the surface of the nanoparticle immersed in water are generally nearer to bulk values compared to the nanoparticle in vacuum. This is because the water provides the additional coordination and therefore the surface ions do not relax markedly into the surface. Consequently the electrostatic potentials of surface oxygen ions are lower and therefore they can be more easily extracted from the surface resulting in a more catalytically active nanoparticle. The origin of the difference is therefore attributed to the interaction between the surface ions and water, which is dipolar.

The simulations suggest that polar solvents would exact a greater change in reactivity compared to immersion non-polar solvents. This has important implications for nanoparticles exploited for biomedicinal applications because the molecular environment, and especially pH, associated with the various bodily compartments in which they reside, will likely impact
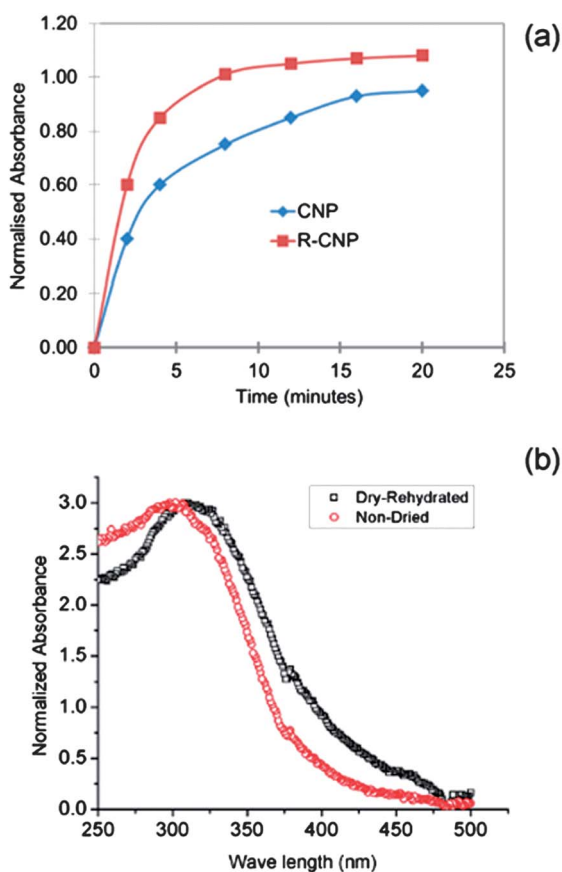
Fig. 9 (a) Activity of ceria nanoparticles towards superoxide radical scavenging for as-prepared ceria nanoparticles (CNP) and the same batch of ceria nanoparticles after drying and rehydrating (R-CNP). (b) UV-Vis spectra of non-dried (CNP) and dried-rehydrated (R-CNP).

upon their reactivity. In particular, our simulations predict that as the nanoparticles move between different environments, so their reactivity will change.

Previous simulations on ceria nanoparticles involved a full ionic model.[33] Here, we use a partial charge model, which is able to better reflect the partial ionicity of the material. We observe some changes with using different potential models. Perhaps the biggest difference is that with partial charge model, the nanoparticle comprises less (we found none) point defects, such as vacancies, within the body of the nanoparticle.

A limitation of empirical modelling is the challenge associated with simulating the charge distribution of nanoceria and its effect on molecular adsorption; the inclusion of localised charge (via Ce^{3+} species substituting for Ce^{4+}) into the model can provide some insight, but is sometimes inadequate. In particular, previous DFT studies have revealed that there is a driving force towards the dissociative adsorption of water at ceria surfaces.[14,28] Here, the adsorption of –OH species onto reduced ceria surfaces is markedly different compared to the adsorption of H_2O onto the surface. And while empirical models used to describe dissociated molecular species and considerations of 'pH' are likely to be developed in the future, simulations using, for example, DFT approximations are better able to capture the charge distribution. It is therefore pertinent to question the use of empirical modelling in such areas. However, a limitation with DFT is its considerable computational expense, which prohibits the direct simulation of, for example, a 10 nm diameter ceria nanoparticle. Moreover, the empirical simulations presented here reveal that simulating the whole nanoparticle is necessary to unravel the behaviour. In particular, our empirical simulations reveal that the detailed atomistic structural complexity of the nanoparticle, including morphology, surfaces exposed, steps edges, corners, grain-boundaries and dislocations play a pivotal role in the surface activity and act synergistically to influence the local activity. Our argument is supported by observing that not all oxygen atoms on the {100} surface of the ceria nanoparticle are labile, conversely, some oxygen atoms occupying positions on {111} surfaces are weakly bound at the surface (see Fig. 6). Accordingly, generalised statements such as '{100} surfaces are more active towards oxygen release compared to {111}' can prove disingenuous; rather the detailed and complex atomistic configuration drives the activity.

At present owing to the computational cost, DFT is limited to simulating artificially symmetric surfaces and therefore cannot capture the potentially profound influence that a neighbouring grain-boundary or dislocation might have on the charge distribution and nanoparticle–solvent interactions. Accordingly, to further our understanding in these areas a combination of both empirical and ab initio simulation is required; each providing complementary information. However, even the combination of computational techniques remains inadequate for this present study. In particular, experimentally, we found that the process of drying and rehydrating ceria nanoparticles reduced their propensity towards superoxide radical scavenging, which was attributed, in part, to a change in the redox chemistry of the ceria nanoparticles. Our results therefore show that not only do the molecular environments, in which the nanomaterials reside, play a key role, but also their transport pathways and environment history. At present, it is not possible to reconcile the relationship between this experimental observation and simulation. In particular, it is doubtful (with the current maturity of empirical and ab initio simulation techniques) that simulating the drying and rehydration process using either or both computational techniques would uncover this unexpected result. It is therefore the combination of techniques that is required, where each technique reveals part of the puzzle that is difficult or intractable using alternative means.

Conclusion

Atomistic simulations predict that the chemical activity of ceria nanoparticles, towards surface oxygen release, increases when the nanoparticle is immersed in water. This is because the water helps saturate under-coordinated surface ions, reducing their propensity to relax into the surface and bind more tightly to subsurface atoms. In addition, our calculations indicate that highly reduced nanoparticles ($Ce^{3+}/Ce^{4+} = 0.6$) are more active towards oxygen release compared to nanoparticles with $Ce^{3+}/Ce^{4+} = 0.02$.

We show how MD simulation and experiment can be used directly to predict how the molecular environment in which a nanoparticle resides, together with the transport pathway, can influence the structure and reactivity of the nanomaterial; a first step in formulating predictive tools to determine the reactivity of nanomaterials in medicinal applications.

Acknowledgements

References

1 K. Zhou and Y. Li, *Angew. Chem., Int. Ed.*, 2012, **51**, 602–613.

2 A. J. Jacobson, *Chem. Mater.*, 2010, **22**, 660–674.

3 X. D. Feng, D. C. Sayle, Z. L. Wang, M. S. Paras, B. Santora, A. C. Sutorik, T. X. T. Sayle, Y. Yang, Y. Ding, X. D. Wang and Y. S. Her, *Science*, 2006, **312**, 1504–1508.

4 A. Asati, S. Santra, C. Kaittanis, S. Nath and J. M. Perez, *Angew. Chem., Int. Ed.*, 2009, **48**, 2308–2312.

5 A. S. Karakoti, S. Singh, A. Kumar, M. Malinska, S. V. N. T. Kuchibhatla, K. Wozniak, W. T. Self and S. Seal, *J. Am. Chem. Soc.*, 2009, **131**, 14144–14145.

6 S. Das, S. Singh, J. M. Dowding, S. O. A. Kumar, T. X. T. Sayle, S. Saraf, C. R. Patra, N. E. Vlahakis, D. C. Sayle, W. T. Self and S. Seal, *Biomaterials*, 2012, **33**, 7746–7755.

7 G. Mobus, Z. Saghi, D. C. Sayle, U. M. Bhatta, A. Stringfellow and T. X. T. Sayle, *Adv. Funct. Mater.*, 2011, **21**, 1971–1976.

8 H. Z. Zhang, B. Chen, Y. Ren, G. A. Waychunas, J. F. Banfield, *et al.*, *Phys. Rev. B: Condens. Matter Mater. Phys.*, 2010, **81**, 125444–125450.

9 H. Zhang, B. Gilbert, F. Huang and J. F. Banfield, *Nature*, 2003, **424**, 1025–1029.

10 A. G. Stack, P. Raiteri and J. D. Gale, *J. Am. Chem. Soc.*, 2012, **134**, 11–14.

11 W. J. Stark, *Angew. Chem., Int. Ed.*, 2011, **50**, 1242–1258.

12 T. X. T. Sayle, M. Cantoni, U. M. Bhatta, S. C. Parker, S. R. Hall, G. Moebus, M. Molinari, D. Reid, S. Seal and D. C. Sayle, *Chem. Mater.*, 2012, **24**, 1811–1821.

13 A. Pedone, M. Gianluca Malavasi, C. Menziani, A. N. Cormack and U. Segre, *J. Phys. Chem. B*, 2006, **110**, 11780–11795.

14 M. Molinari, S. C. Parker, D. C. Sayle and M. S. Islam, *J. Phys. Chem. C*, 2012, **116**, 7073–7082.

15 W. D. Cornell, P. Cieplak, C. I. Bayly, I. R. Gould, R. M. Merz, D. M. Ferguson, D. C. Spellmeyer, T. Fox, J. W. Caldwell and P. A. Kollman, *J. Am. Chem. Soc.*, 1995, **117**, 5179–5197.

16 J. D. Gale, *Z. Kristallogr.*, 2005, **220**, 552–554.

17 G. W. Watson, E. T. Kelsey, N. H. deLeeuw, D. J. Harris and S. C. Parker, *J. Chem. Soc., Faraday Trans.*, 1996, **92**, 433–438.

18 W. Smith and T. R. Forester, DL_POLY, Copyright by the Council for the Central Laboratory of the Research Councils, Daresbury Laboratory, Daresbury, Warrington, UK, 1996, http://www.cse.clrc.ac.uk/msi/software/DL_POLY/.

19 W. Humphrey, A. Dalke and K. Schulten, *J. Mol. Graphics*, 1996, **14.1**, 33–38.

20 K. Momma and F. J. Izumi, *Appl. Crystallogr.*, 2008, **41**, 653–658.

21 T. X. T. Sayle, S. C. Parker and C. R. A. Catlow, *Surf. Sci.*, 1994, **316**, 329–336.

22 A. Migani, G. N. Vayssilov, S. T. Bromley, F. Illas and K. M. Neyman, *J. Mater. Chem.*, 2010, **20**, 10535–10546.

23 S. Patil, S. C. Kuiry, S. Seal and R. Vanfleet, *J. Nanopart. Res.*, 2002, **4**, 433–438; S. Patil, A. Sandberg, E. Heckert, W. Self and S. Seal, *Biomaterials*, 2007, **28**, 4600–4607.

24 H. X. Mai, L. D. Sun, Y. W. Zhang, R. Si, W. Feng, H. P. Zhang, H. C. Liu and C. H. Yan, *J. Phys. Chem. B*, 2005, **109**, 24380–24385.

25 S. Vyas, R. W. Grimes, D. H. Gay and A. L. Rohl, *J. Chem. Soc., Faraday Trans.*, 1998, **94**, 427–434.

26 H. X. Xu, R. K. Behera, Y. L. Wang, F. Ebrahimi, S. B. Sinnott, E. D. Wachsman and S. R. Phillpot, *Solid State Ionics*, 2012, **181**, 551–556.

27 A. Walsh, S. M. Woodley, C. R. A. Catlow and A. A. Sokol, *Solid State Ionics*, 2011, **184**, 52–56.

28 M. Nolan, S. Grigoleit, D. C. Sayle, S. C. Parker and G. W. Watson, *Surf. Sci.*, 2005, **576**, 1–3.

29 K. Yoshida, T. Kawai, T. Nambara, S. Tanemura, K. Saitoh and N. Tanaka, *Nanotechnology*, 2006, **17**, 3944–3950.

30 J. H. Harding, *Surf. Sci.*, 1999, **422**, 87.

31 T. X. T. Sayle, S. C. Parker and D. C. Sayle, *J. Mater. Chem.*, 2006, **16**, 1067–1081.

32 N. Shibata, F. Oba, T. Yamamoto and Y. Ikuhara, *Philos. Mag.*, 2004, **84**, 2381–2415.

33 T. X. T. Sayle, S. C. Parker and D. C. Sayle, *Chem. Commun.*, 2004, **21**, 2438–2439.